minerals

MDPI

Article

Improving Marine Mineral Delineation with Planar Self-Potential Data and Bayesian Inversion

Lijuan Zhang [1,2], Shengfeng Feng [1,2,*], Shengcai Xu [1,2], Dingyu Huang [1,2], Hewang Li [1,2], Ying Su [1,2] and Jing Xie [3,*]

[1] School of Architecture and Electrical Engineering, Hezhou University, Hezhou 542899, China; zhanglijuan@hzxy.edu.cn
[2] Guangxi University Engineering Research Center for Green and Low-Carbon Urban Regeneration Construction, Hezhou University, Hezhou 542899, China
[3] School of Geosciences and Info-Physics, Central South University, Changsha 410083, China
* Correspondence: fengshengfeng@hzxy.edu.cn (S.F.); jingpku@pku.edu.cn (J.X.)

Abstract

The exploration of marine minerals, essential for sustainable development, requires advanced techniques for accurate resource delineation. The self-potential (SP) method, sensitive to mineral polarization, has been increasingly deployed using autonomous underwater vehicles. This approach enables dense planar SP data acquisition, offering the potential to reduce inversion uncertainties through enhanced data volume. This study investigates the benefits of inverting planar SP datasets for improving the spatial delineation of subsurface deposits. An analytical solution was derived to describe SP responses of spherical polarization models under a planar measurement grid. An adaptive Markov chain Monte Carlo algorithm within the Bayesian framework was employed to quantitatively assess the constraints imposed by the enriched dataset. The proposed methodology was validated through two synthetic cases, along with a laboratory-scale experiment that monitored the redox process of a spherical iron–copper model. The results showed that, compared to single-line data, the planar data reduced the average error in parameter means from 10.9% and 6.4% to 4.1% and 1.7% for synthetic and experimental cases, respectively. In addition, the 95% credible intervals of model parameters narrowed by nearly 50% and 40%, respectively.

Keywords: self-potential; marine minerals; Bayesian inversion; Markov chain Monte Carlo

check for updates

Academic Editor: Saulo Pomponet Oliveira

Received: 18 November 2025
Revised: 11 December 2025
Accepted: 17 December 2025
Published: 18 December 2025

Citation: Zhang, L.; Feng, S.; Xu, S.; Huang, D.; Li, H.; Su, Y.; Xie, J. Improving Marine Mineral Delineation with Planar Self-Potential Data and Bayesian Inversion. *Minerals* **2025**, *15*, 1330. https://doi.org/10.3390/min15121330

Copyright: © 2025 by the authors. Licensee MDPI, Basel, Switzerland. This article is an open access article distributed under the terms and conditions of the Creative Commons Attribution (CC BY) license (https://creativecommons.org/licenses/by/4.0/).

1. Introduction

The seabed hosts substantial metallic mineral resources with commercial exploitation potential, including polymetallic nodules, cobalt-rich crusts, and polymetallic sulfides, which constitute critical material foundations for sustainable development [1,2]. As terrestrial reserves dwindle, international interest in exploring and developing these marine resources has grown significantly in recent years [3–5]. In this context, developing accurate and efficient exploration technologies for marine minerals is of critical importance and practical relevance.

Geophysical methods play a key role in marine mineral exploration. Commonly used techniques include active methods, such as induced polarization [6,7], resistivity surveying [8,9], and electromagnetic methods [10–12], as well as passive approaches like gravity and magnetic surveys [13,14] and the self-potential (SP) method [15–17]. Among these, the SP method is particularly sensitive to subsurface electrochemical gradients. It can directly reflect redox gradients generated during the natural polarization of buried

deposits by measuring SP signals above the seafloor [18,19]. Due to this capability, the SP method has gained increasing attention and application in recent years for exploring marine metallic mineral resources, particularly seafloor massive sulfides [15–18].

In terrestrial environments, SP measurements are typically conducted along single line due to constraints such as complex topography and limited acquisition efficiency [20–22]. However, the small datasets obtained from such single-line surveys often lead to significant challenges in inversion and interpretation, including strong non-uniqueness of solutions and difficulties in accurately characterizing the 3D spatial structure of subsurface targets [21–23]. In contrast, recent advances in marine exploration have introduced novel SP acquisition systems based on autonomous underwater vehicles, which enable efficient collection of SP data over planar grids composed of multiple survey lines [24–27]. This progress makes it essential to quantitatively evaluate how planar data inversion improves the delineation of subsurface ore structures compared to single-line inversion.

This study aims to quantitatively analyze the effectiveness of inverting SP data from planar surveys in improving the structural constraints of subsurface deposits. Building upon the analytical solution for a spherical polarization model under a single survey line, we extended the model by incorporating coordinates from adjacent survey lines to derive an analytical solution suitable for planar acquisitions. A Markov chain Monte Carlo (MCMC) algorithm within the Bayesian framework was then employed for stochastic inversion, quantifying the constraint ability of different data volumes on parameter uncertainties. The quantitative investigation began with synthetic cases. Furthermore, a physical simulation experiment was designed to model the redox process of metallic minerals. We employed a multi-channel SP monitoring platform to record SP data generated during the redox process of a spherical iron–copper model, enabling evaluating the positive effect of planar SP measurements for delineating subsurface ore structures.

2. Theory

2.1. Analytical Solution for Planar Acquisition

There are two primary numerical approaches for SP forward modeling. The first involves solving the governing Poisson equation using numerical methods such as the finite element [28], finite difference [29], finite volume [30], or related coupled techniques. In contrast, the second approach relies on analytical solutions, where subsurface targets are idealized as regular geometric shapes, allowing direct calculation of the surface SP responses. These analytical solutions, enabling near-instantaneous forward modeling, characterize SP anomalies based on the positions of the polarization poles, the dipole moment density, and the geometry of the source body. Commonly used idealized shapes include spheres, cylinders, and sheet-like structures, which simplify the representation of natural polarization for minerals.

This study takes the spherical polarization model as an example. For the single-line acquisition, the SP anomaly $\varphi(x)$ (mV) along a profile passing over the center of a sphere can be expressed as [20]:

$$\varphi(x) = K\frac{(x - x_0)\cos\theta + h\sin\theta}{\left[(x - x_0)^2 + h^2\right]^q} \tag{1}$$

where K is the polarization parameter (mV), x_0 is the x-coordinate of the sphere center (m), h is the depth to the center (m), θ is the polarization angle, and q = 1.5 is the shape factor.

In marine environments, measurements utilizing autonomous underwater vehicles can efficiently acquire SP data over planar surveys. As illustrated in Figure 1, based on

Equation (1), the expression for SP applicable to planar surveys can be derived. The SP value $\varphi(x, y, z)$ at point (x, y, z) on the seafloor can be expressed as:

$$\varphi(x,y,z) = K\frac{|z - z_0|}{\left[(x - x_0)^2 + (y - y_0)^2 + (z - z_0)^2\right]^q} \quad (2)$$

where (x_0, y_0, z_0) denotes the spatial coordinates of the sphere center. Note that this model is specifically applicable to a spherical model with vertical polarization. However, by modifying the shape factor, it can also be adapted to model a vertically polarized cylinder (when $q = 0.5$).

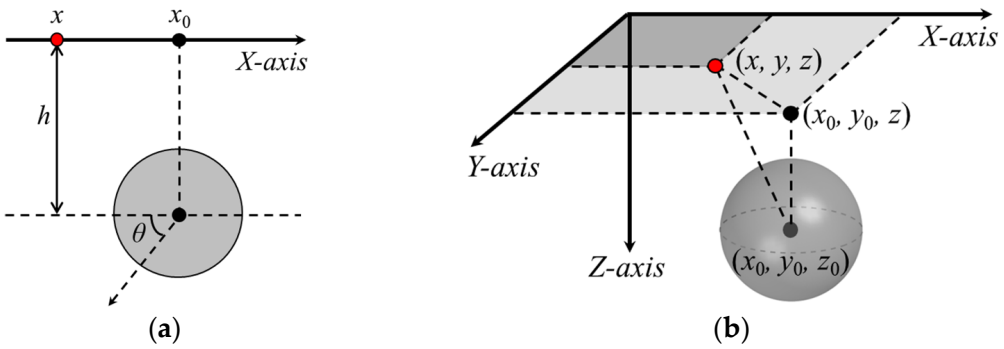


Figure 1. Schematic diagram for data acquisition: (**a**) single-line acquisition; (**b**) planar acquisition.

2.2. Uncertainty Inversion by MCMC

Corresponding to these two forward modeling schemes discussed above, the quantitative interpretation approaches for SP data are, respectively, (1) gradient-based inversion, specifically referring to algorithms that require repeated forward modeling of complex resistivity models; and (2) global optimization inversion, typically based on analytical solutions describing the natural polarization of simple geometric bodies. The former is suitable for complex models but is highly dependent on initial models and computationally intensive [16]. In mineral exploration, SP data interpretation often employs the later approach to infer the model parameters related to deposit distributions. These models have a few parameters, making global optimization algorithms commonly used for such inversion. Widely adopted algorithms include particle swarm optimization [31], simulated annealing [32], and the whale optimization algorithm [33].

Given the high non-uniqueness in SP inversion, quantifying the uncertainty of model parameters can help address the ill-posed nature [34]. In this study, we employed an adaptive MCMC algorithm within the Bayesian framework to perform uncertainty inversion of SP data. This approach facilitates the investigation of parameter uncertainties and correlations [34,35].

The Bayesian approach for parameter estimation is typically implemented with the aid of MCMC, which utilizes a random walk strategy to generate samples that follow the posterior distribution of model parameters [36]. To maintain detailed balance and ergodicity, this study employed the adaptive Metropolis algorithm [37] to perform MCMC sampling. The implementation of the adaptive Metropolis algorithm follows the procedure outlined below [34,35]:

1. Initialization:

   Assume k model vectors $\mathbf{m}^0, \mathbf{m}^1, \ldots, \mathbf{m}^{k-1}$ have been sampled.

2. Candidate sampling:

To obtain the next model vector $\mathbf{m}^k$, a candidate vector $\mathbf{m}_{cd}$ is sampled from a Gaussian proposal distribution with the mean value at the current model $\mathbf{m}^{k-1}$ and with the covariance matrix $\mathbf{C}^k$. $\mathbf{C}^k$ can be expressed as:

$$\mathbf{C}^k = \begin{cases} \mathbf{C}^0 & k \le k_0 \\ s_n \mathbf{K}^k + s_n \varepsilon \mathbf{I} & k > k_0 \end{cases} \tag{3}$$

where $\mathbf{K}^k = \mathrm{cov}(\mathbf{m}^0, \mathbf{m}^1, \ldots, \mathbf{m}^{k-1})$, $s_n = 2.4^2/n$ is a scaling parameter (with n being the dimension of $\mathbf{m}_{cd}$), ε is a small positive value, $\mathbf{I}$ denotes an $n \times n$ identity matrix, and k_0 defines the burn-in period.

3. Acceptance criterion:

Determine whether the candidate vector $\mathbf{m}_{cd}$ is accepted (i.e., $\mathbf{m}^k = \mathbf{m}_{cd}$) or rejected (i.e., $\mathbf{m}^k = \mathbf{m}^{k-1}$). The acceptance probability is given by:

$$\beta(\mathbf{m}^{k-1}, \mathbf{m}_{cd}) = \min\left[\frac{\pi(\mathbf{m}_{cd})}{\pi(\mathbf{m}^{k-1})}, 1\right] \tag{4}$$

In the adaptive Metropolis algorithm, the ratio $\pi(\mathbf{m}_{cd})/\pi(\mathbf{m}^{k-1})$ can be describes as:

$$\frac{\pi(\mathbf{m}_{cd})}{\pi(\mathbf{m}^{k-1})} = \frac{P_0(\mathbf{m}_{cd})P(\mathbf{d}|\mathbf{m}_{cd})}{P_0(\mathbf{m}^{k-1})P(\mathbf{d}|\mathbf{m}^{k-1})} \tag{5}$$

where the likelihood $P(\mathbf{d} \mid \mathbf{m}_{cd})$ or $P(\mathbf{d} \mid \mathbf{m}^{k-1})$ quantifies the fit between the observed data $\mathbf{d}$ and the data predicted from $f(\mathbf{m}_{cd})$ or $f(\mathbf{m}^{k-1})$, with f denoting the forward operator. The prior distribution $P_0(\mathbf{m}_{cd})$ or $P_0(\mathbf{m}^{k-1})$ is typically defined by prescribed parameter bounds:

$$P_0(\mathbf{m}_{cd}) = \begin{cases} 1 & \mathbf{m}_{cd} \in [\mathbf{a}, \mathbf{b}] \\ 0 & \mathbf{m}_{cd} \notin [\mathbf{a}, \mathbf{b}] \end{cases} \tag{6}$$

where $[\mathbf{a}, \mathbf{b}]$ is the prior bounds for $\mathbf{m}_{cd}$.

4. Iteration:

Repeat the steps above until k reaches a predefined threshold.

3. Synthetic Case Validation

3.1. Laboratory-Scale Case

In the first synthetic case, the model is established based on the experimental scale. The sphere center is set at coordinates (50 cm, 25 cm, −25 cm), with a polarization intensity of 5 mV. The measurement points cover a range of 0~100 cm along the x-axis and 0~50 cm along the y-axis, with a spacing of 5 cm. To unify the degrees of freedom, the parameter y_0 = 25 cm is treated as known. Thus, the model parameters for both the single-line and planar surveys are defined as [x_0 = 50 cm, z_0 = −25 cm, K = 5 mV, q = 1.5]. The initial model is [30 cm, −15 cm, 10 mV, 1.2], while the initial covariance during the burn-in period is configured as 5% of the prior range for each parameter. Each inversion run consists of 50,000 forward simulations, with the first 20,000 iterations designated as the burn-in phase. The inversion results under 10% and 20% noise levels are, respectively, summarized in Tables 1 and 2, where the mean values and 95% credible intervals of the MCMC-inferred parameters are computed from the last 30,000 samples. The computational time for a single inversion run is approximately 1.5 s.

The MCMC inversion results indicate that (1) the parameter x_0 is estimated with the highest accuracy in terms of the posterior mean and also exhibits the narrowest 95% credible

interval, indicating the highest sensitivity; (2) the parameter K shows the lowest confidence level, which can be attributed to the fact that its value is jointly influenced by multiple parameters controlling the amplitude; (3) statistical analysis of the posterior samples reveals that, compared to the single-line data, the planar data leads to an average reduction of nearly 50% in the width of the 95% credible interval, while the mean relative difference in the estimated parameters decreases from 13.5% to 3.5% in the 10% noise case and from 9.6% to 6.1% in the 20% noise case; and (4) higher noise levels increase the sampling acceptance rate, resulting in a widening of the average 95% credible intervals from 48.9% and 19.9% in the 10% noise case to 75.9% and 36.6% in the 20% noise case, respectively. These findings demonstrate the superior capability of planar SP data in delineating the distribution of subsurface targets.

Table 1. Summary of the MCMC estimated model parameters obtained from the lab-scale synthetic model under 10% noise level. In the 5th and 6th columns, the estimated mean values of model parameters are highlighted in bold, followed by the associated relative differences presented within parentheses; the 95% credible intervals are enclosed in square brackets, and the relative lengths of them are indicated in italics.

Parameter	True Value	Prior Mean	Prior Bounds	Inversion Results of Single-Line Data	Inversion Results of Planar Data
x_0 (cm)	50	30	0~100	**50.24** (0.5%) [49.90, 50.54] *1.3%*	**49.95** (1.0%) [49.57, 50.12] *1.1%*
z_0 (cm)	−25	−15	−50~0	**−22.87** (8.5%) [−26.77, −19.81] *27.8%*	**−24.53** (1.9%) [−26.03, −23.34] *10.8%*
K (mV)	5	10	0~20	**6.81** (36.2%) [3.49, 10.02] *130.6%*	**5.42** (8.4%) [4.35, 6.93] *51.6%*
q (-)	1.5	1.2	1~2	**1.37** (8.7%) [1.15, 1.69] *36.0%*	**1.46** (2.7%) [1.34, 1.58] *16.0%*

Table 2. Summary of the MCMC estimated model parameters obtained from the lab-scale synthetic model under 20% noise level. In the 5th and 6th columns, the estimated mean values of model parameters are highlighted in bold, followed by the associated relative differences presented within parentheses; the 95% credible intervals are enclosed in square brackets, and the relative lengths of them are indicated in italics.

Parameter	True Value	Prior Mean	Prior Bounds	Inversion Results of Single-Line Data	Inversion Results of Planar Data
x_0 (cm)	50	30	0~100	**49.84** (0.3%) [48.94, 50.50] *3.1%*	**49.98** (0.4%) [49.49, 50.68] *2.4%*
z_0 (cm)	−25	−15	−50 0	**−24.11** (3.6%) [−31.75, −19.01] *51.0%*	**−24.47** (2.1%) [−28.37, −21.65] *26.9%*
K (mV)	5	10	0~20	**6.45** (29.0%) [2.59, 12.07] *189.6%*	**5.90** (18.0%) [4.11, 8.59] *89.6%*
q (-)	1.5	1.2	1~2	**1.42** (5.3%) [1.07, 1.97] *60.0%*	**1.44** (4.0%) [1.24, 1.65] *27.3%*

Figures 2 and 3 present histograms of the parameter distributions obtained from MCMC sampling, along with the correlations between parameters. The following observations can be made: (1) The histograms visually reflect the uncertainty in the model parameters; (2) The parameter q exhibits strong negative correlations with z_0 and K, with correlation coefficients of −0.9855 and −0.9803 in the 10% noise case and −0.9692 and −0.9200 in the 20% noise case for the single-line data, and −0.8780 and −0.9805 in the 10% noise case and −0.9357 and −0.9723 in the 20% noise case for the planar data, respectively.

This behavior is consistent with the model formulation, in which the contribution of q to SP values is the same as that of z_0 and K (Note that this relation holds when the base of the denominator is less than 1 and its exponent is greater than 1); (3) A positive correlation is observed between K and z_0, with correlation coefficients of 0.9568 and 0.8302 in the 10% noise case and 0.8676 and 0.8583 in the 20% noise case. This apparent positive correlation stems from the negative value of z_0, which reverses the inherent correlation direction.

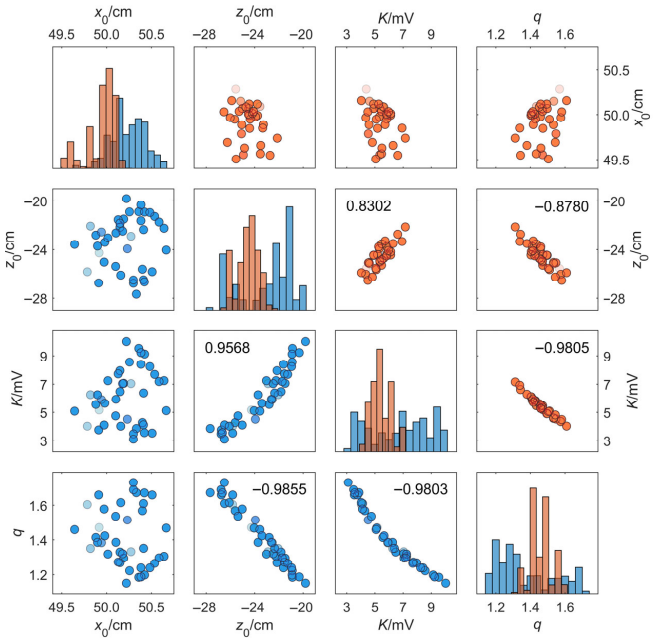


Figure 2. MCMC solutions from synthetic SP data with a noise level of 10%; The on-diagonal plots represent the posterior probability distribution of model parameters, and the off-diagonal scatterplots represent the pairwise correlations in the MCMC sampling (blue for single-line data and orange for planar data).

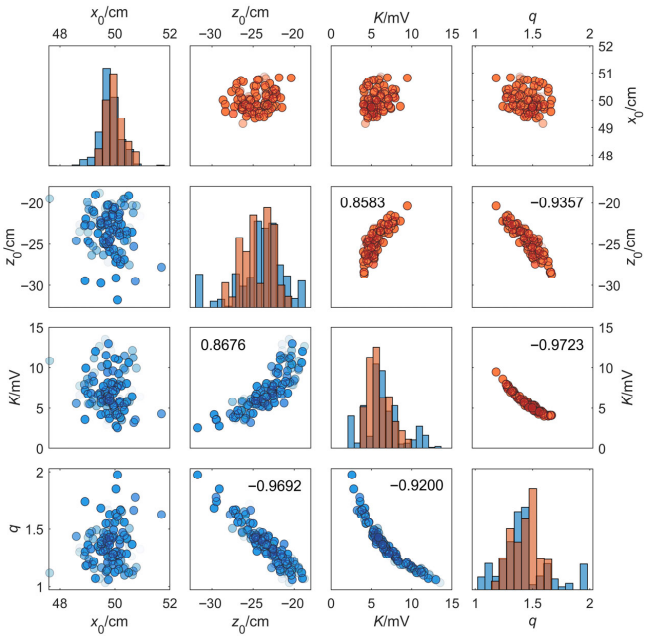


Figure 3. MCMC solutions from synthetic SP data with a noise level of 20%; The on-diagonal plots represent the posterior probability distribution of model parameters, and the off-diagonal scatterplots represent the pairwise correlations in the MCMC sampling (blue for single-line data and orange for planar data).

3.2. Field-Scale Case

In the second synthetic case, the model is established based on a field scale with two spherical deposits. The sphere centers are, respectively, set at coordinates (60 m, 50 m, −15 m) and (140 m, 50 m, −15 m), with a polarization intensity of 1000 mV. The measurement points cover a range of 0~200 m along the x-axis and 0~100 m along the y-axis, with a spacing of 10 m. To unify the degrees of freedom, the parameter y_0 = 50 m is treated as known. Thus, the model parameters for both the single-line and planar surveys are defined as [x_{0_1} = 60 m, x_{0_2} = 140 m, z_{0_1} = −15 m, z_{0_2} = −15 m, $K_{_1}$ = 1000 mV, $K_{_2}$ = 1000 mV, $q_{_1}$ = 1.5, $q_{_2}$ = 1.5], where the subscripts 1 and 2, respectively, represent the two spherical deposits. The initial model is [80 m, 120 m, −10 m, −10 m, 600 mV, 600 mV, 1.2, 1.2], while the initial covariance during the burn-in period is configured as 5% of the prior range for each parameter. Each inversion run consists of 100,000 forward simulations, with the first 50,000 iterations designated as the burn-in phase. The inversion results under 10% noise level are summarized in Table 3, where the mean values and 95% credible intervals of the MCMC-inferred parameters are computed from the last 50,000 samples. The computational time for a single inversion run is approximately 10 s.

Table 3. Summary of the MCMC estimated model parameters obtained from the field-scale synthetic model under 10% noise level. In the 5th and 6th columns, the estimated mean values of model parameters are highlighted in bold, followed by the associated relative differences presented within parentheses; the 95% credible intervals are enclosed in square brackets, and the relative lengths of them are indicated in italics.

Parameter	True Value	Prior Mean	Prior Bounds	Inversion Results of Single-Line Data	Inversion Results of Planar Data
x_{0_1} (m)	60	80	0~200	**60.26** (0.4%) [59.12, 60.97] *3.1%*	**60.09** (0.2%) [59.45, 60.65] *2.0%*
x_{0_2} (m)	140	120	0~200	**140.19** (0.1%) [139.22, 140.62] *1.0%*	**140.61** (0.4%) [139.77, 140.69] *0.7%*
z_{0_1} (m)	−15	−10	−50~0	**−14.26** (4.9%) [−15.27, −13.74] *10.2%*	**−14.63** (2.5%) [−15.19, −14.47] *4.8%*
z_{0_2} (m)	−15	−10	−50~0	**−14.54** (3.1%) [−15.23, −13.88] *9.0%*	**−14.78** (1.5%) [−15.32, −14.41] *6.1%*
$K_{_1}$ (mV)	1000	600	500~1500	**642.53** (35.7%) [514.82, 1060.76] *54.6%*	**934.63** (6.5%) [892.38, 1048.48] *15.6%*
$K_{_2}$ (mV)	1000	600	500~1500	**754.58** (24.5%) [534.02, 893.11] *35.9%*	**909.78** (9.0%) [866.97, 1109.30] *24.2%*
$q_{_1}$ (-)	1.5	1.2	1~2	**1.43** (4.7%) [1.21, 1.62] *27.3%*	**1.49** (0.7%) [1.37, 1.64] *18.0%*
$q_{_2}$ (-)	1.5	1.2	1~2	**1.45** (3.3%) [1.28, 1.59] *20.7%*	**1.48** (1.3%) [1.35, 1.57] *14.7%*

Statistical analysis of the field-scale case shows a conclusion consistent with that of the laboratory-scale cases: planar data provides stronger constraints on parameter recovery. This improvement is evident in both the accuracy of the mean model (the average error decreases from 9.6% to 2.8%) and a smaller uncertainty assessed by the 95% credible interval (the average relative length decreases from 20.2% to 10.8%). The main difference lies in the sampling correlations between parameters, which are primarily observed between q and K and show a positive correlation (average correlation coefficient of 0.9253). This is because the base of the denominator is greater than 1 and the exponent $q > 1$, causing the contribution of q to the SP value to oppose that of K. Additionally, in the single-line test, the underestimation of K is related to the underestimation of q.

4. Laboratory Experiment Validation

4.1. Laboratory Experiment

Laboratory-scale physical simulation provides an effective approach for investigating SP signals within the framework of the geobattery model [38]. In this study, a spherical iron–copper model was used to simulate the natural polarization of a metallic ore body. A multi-channel SP monitoring platform was employed to measure the SP signals generated at the anode of the geobattery model. The experimental setup mainly consists of the following components: (1) a 192-channel SP data logger with a sensitivity of 0.01 mV; (2) 120 micro-button sintered Ag–AgCl non-polarized electrodes, each 6 mm in diameter, fixed in an insulated polymer plastic holder and arranged in a 24 × 5 grid with spacings of 4 cm and 6 cm, respectively; (3) a plexiglass tank with dimensions of 100 cm × 50 cm × 50 cm (*x*-, *y*-, *z*-axis); and (4) iron and copper hemispheres, each 15 cm in diameter. This platform has been successfully applied in several previous SP monitoring experiments, including studies on iron corrosion, fluid migration, and microbial activities [39].

The redox monitoring experiment in this study was conducted in tap water for the following reasons: (1) Tap water contains abundant oxygen and conductive ions, which promote faster and more active redox reactions and facilitate the formation of an external circuit; (2) The nearly homogeneous medium helps minimize noise disturbances and interference from other types of SP signals (e.g., diffusion potentials and streaming potentials), resulting in a more well-defined redox-induced SP anomaly; (3) The transparent nature of both water and the plexiglass tank allows direct visual observation of the dynamic oxidation and corrosion processes occurring at the anode during the experiment.

As shown in Figure 4, the iron hemisphere is positioned at the top with the copper hemisphere at the bottom, resulting in a geobattery configuration where the cathode and anode are reversed compared to the conventional arrangement. This setup offers improved control over the corroded surface and facilitates enhanced observation of Fe^{3+} related rust formation during the experiment.

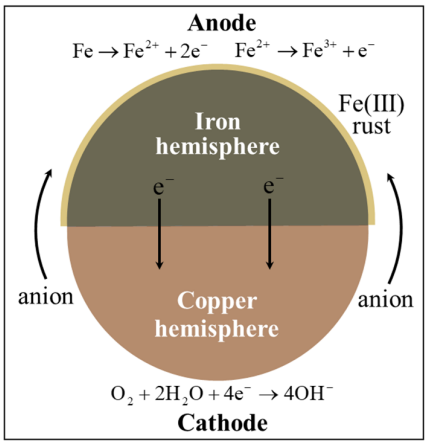


Figure 4. Electron transfer mechanisms and electrochemical half-cell reactions within the geobattery framework.

The electrochemistry underlying the corrosion of the iron hemisphere can be described as follows [40]:

Step 1: At the upper section, iron acts as an electron donor. The rust formation process initiates with the oxidation of iron to ferrous ions (Fe^{2+}) through the following reactions:

$$Fe \rightarrow Fe^{2+} + 2e^{-} \quad (7)$$

$$Fe^{2+} + 2OH^{-} \rightarrow Fe(OH)_2 \quad (8)$$

Step 2: $Fe(OH)_2$ is unstable and undergoes further oxidation to ferric ions (Fe^{3+}), resulting in the formation of rust species such as ferric oxyhydroxide hydrate ($FeOOH \cdot xH_2O$) and ferric oxide hydrate ($Fe_2O_3 \cdot xH_2O$), where x denotes the number of water molecules complexed with the Fe^{3+} oxide:

$$Fe^{2+} \rightarrow Fe^{3+} + e^- \quad (9)$$

$$4Fe(OH)_2 + O_2 \rightarrow 4FeOOH + 2H_2O \quad (10)$$

$$4Fe(OH)_2 + O_2 \rightarrow 2Fe_2O_3 + 4H_2O \quad (11)$$

Step 3: At the lower section, copper facilitates the downward transfer of electrons, while oxygen serves as the electron acceptor according to:

$$O_2 + 2H_2O + 4e^- \rightarrow 4OH^- \quad (12)$$

These redox reaction equations elucidate the electron transfer mechanism involved in the natural polarization of metallic minerals, and provide the theoretical foundation for the physical experiment conducted in this study.

Figure 5 shows the electrode arrangement and numbering system, while Figure 6 presents the experimental setup for the vertical polarization test. The electrode holder was fixed at a height of 35 cm using insulated plastic tubes, with the water level maintained at a height of 40 cm. The reference electrode was placed at a corner of the tank bottom to minimize disturbance from the measurement area. Each set of measurements with the 120-channel electrodes requires approximately 20.48 s. A total of 3977 datasets was recorded throughout the experiment, corresponding to a total duration of approximately 22.62 h. The first 2609 datasets (spanning 14.8 h) and the last 309 datasets were designated as background monitoring. Datasets 2610 to 3668 covered the redox monitoring process, lasting approximately 6 h. During the experiment, the spherical model was positioned in the center of the tank, with its center located approximately 20 cm from the electrode holder and a polarization angle θ of 90°.

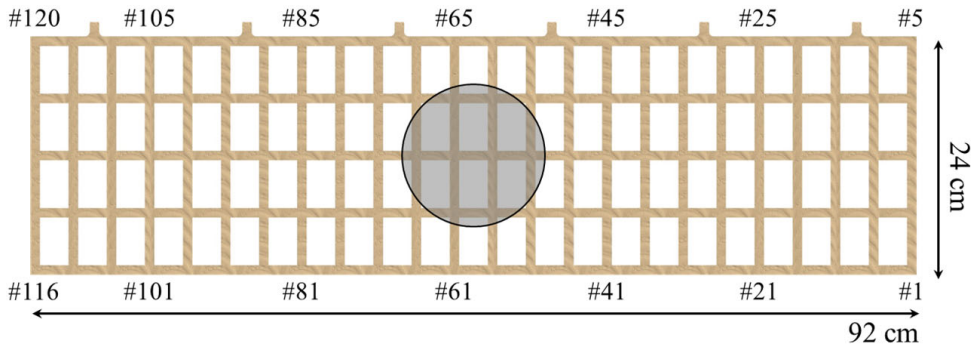


Figure 5. Electrode arrangement and numbering; The gray area indicates the projection of the model.

The raw time-series SP data recorded by electrodes 46 to 75, located above the model, are shown in Figure 7. The following observations were made: (1) During the background monitoring phase, the SP signals remained stable and fluctuated near the zero baseline. (2) After the initiation of the redox experiment, electrodes close to the sphere quickly detected a prominent positive SP anomaly exceeding 40 mV. The signals then stabilized and persisted until the sphere was removed, after which they rapidly declined to the background noise level.

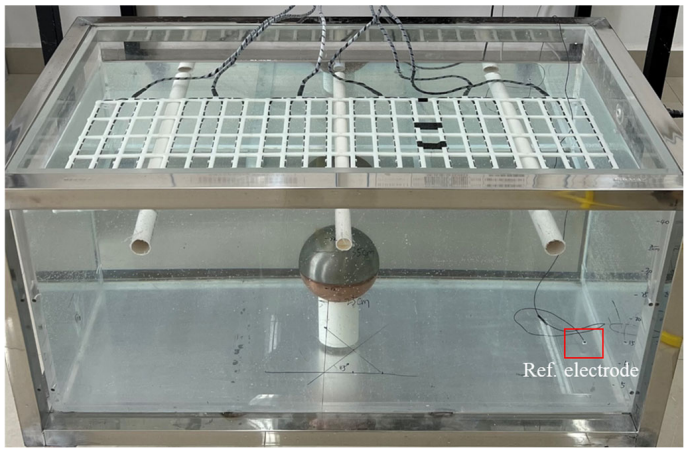


Figure 6. Photograph of the experimental setup.

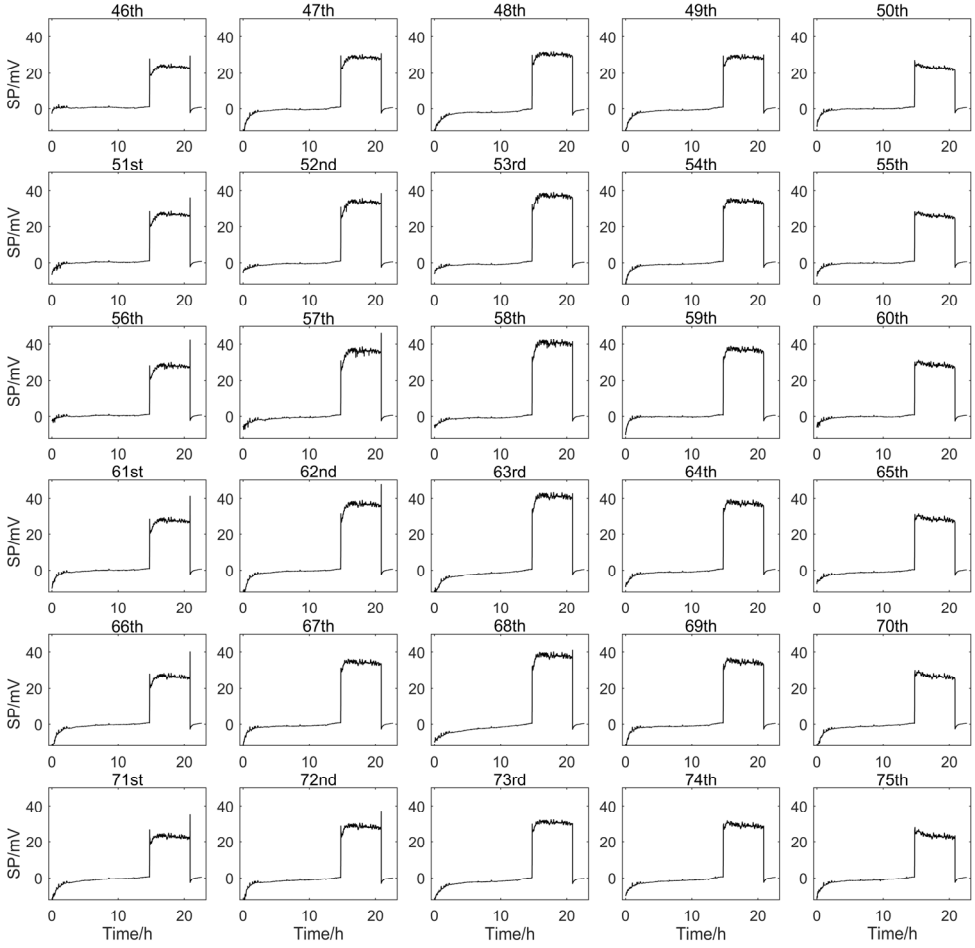


Figure 7. Raw time-series SP data recorded from the electrodes (Nos. 46 to 75) situated above the model.

Figure 8 shows the SP distribution at different time points: 10 h (background monitoring phase), 16.85 h (2 h after placement of the model), and 19.85 h (5 h after placement). The following characteristics were observed: (1) The measured data were of high quality with minimal interference; (2) The anomaly maximum coincided with the projection of the model; (3) The SP field exhibited a symmetric distribution around the anomaly maximum, decaying concentrically with increasing distance.

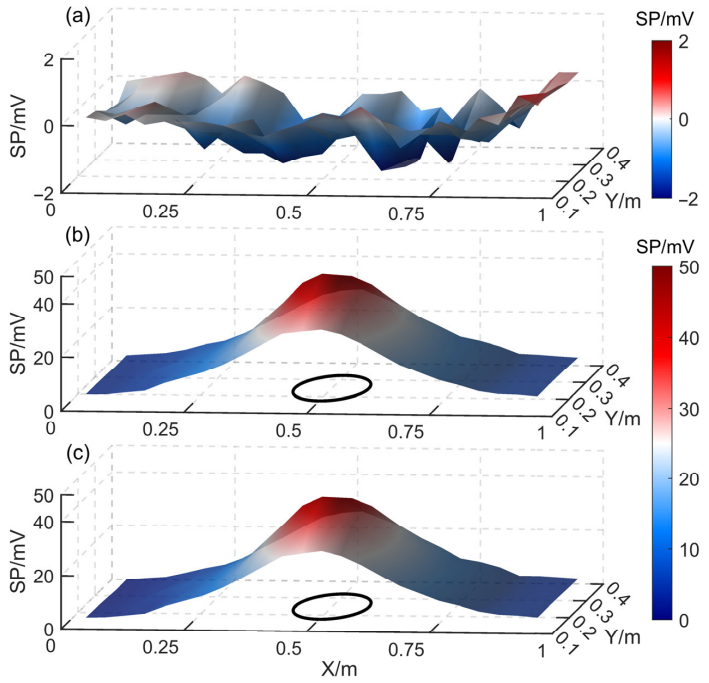
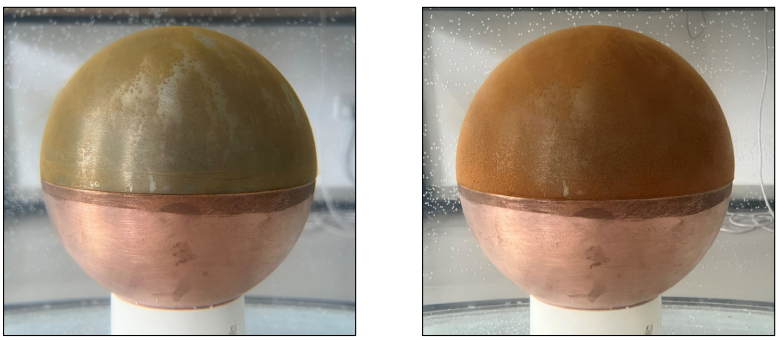


Figure 8. SP distributions at different time points: (**a**) the 10th hour; 2 h (**b**) and 5 h (**c**) after the placement of the model. The black circles indicate the projection of the model.

Figure 9 illustrates the accumulation of Fe^{3+} rust on the iron hemisphere during the experiment, with images captured at 2 h and 5 h after the placement. The corresponding SP signals are shown in Figures 8b and 8c respectively. The following observations were made: after the spherical model was placed in water, Fe^{3+} rust rapidly accumulated on the surface of the iron hemisphere. The rust coverage increased over time and was distributed relatively uniformly. In contrast, the copper hemisphere, which functioned solely as an electron conductor, exhibited no visible change.



(**a**) (**b**)

Figure 9. Photographs of the model at different time points: 2 h (**a**) and 5 h (**b**) after the placement.

4.2. MCMC Inversion

For the MCMC inversion of the experimental data, the measurement taken at the 5th hour after the placement (Figure 8c) was used to estimate parameter uncertainties. The single-line data consisted of measurements from the main survey line electrodes (Nos. 3, 8, 13, . . ., 113, and 118), while the planar grid data comprised all 120 channels. In the experimental configuration, the sphere center was located at (50 cm, 25 cm, −20 cm) with an unknown polarization intensity. The measurement points spanned x = 4~96 cm and y = 13~37 cm, with respective spacings of 4 cm and 6 cm. y_0 = 25 cm was treated as a known parameter. Thus, the model parameters for both the single-line and planar surveys were defined as [x_0 = 50 cm,

z_0 = −20 cm, K (unknown), q = 1.5]. The initial model was set to [30 cm, −10 cm, 10 mV, 1.2], and other MCMC settings were consistent with the first synthetic case.

The mean values and 95% credible intervals of the parameters estimated through MCMC inversion are summarized in Table 4. The results lead to conclusions consistent with those from the synthetic case: (1) The estimate of x_0 achieves the highest accuracy and the lowest uncertainty; (2) Compared to the single-line data, the planar data reduces the average width of the 95% credible interval by nearly 40%, and lowers the mean relative difference of the parameter estimates from 6.4% to 1.7%.

Table 4. Summary of the MCMC estimated model parameters obtained from the laboratory experiment. In the 5th and 6th columns, the estimated mean values of model parameters are highlighted in bold, followed by the associated relative differences presented within parentheses; the 95% credible intervals are enclosed in square brackets, and the relative lengths of them are indicated in italics.

Parameter	True Value	Prior Mean	Prior Bounds	Inversion Results of Single-Line Data	Inversion Results of Planar Data
x_0 (cm)	50	30	0~100	**50.26** (0.5%) [49.56, 51.02] *2.9%*	**50.27** (0.5%) [49.96, 50.98] *2.0%*
z_0 (cm)	−20	−10	−50~0	**−18.68** (6.6%) [−21.96, −14.62] *36.7%*	**−20.63** (3.2%) [−22.71, −17.98] *23.7%*
K (mV)	\	10	0~20	**2.99** [1.36, 5.82]	**2.04** [1.46, 2.97]
q (-)	1.5	1.2	1~2	**1.32** (12.0%) [1.02, 1.62] *40.0%*	**1.48** (1.3%) [1.30, 1.63] *22.0%*

Figure 10 presents the posterior probability distributions of model parameters and their correlation relationships obtained from MCMC sampling. The results are consistent with the findings from the synthetic model: parameter q shows negative correlations with z_0 and K, with correlation coefficients of −0.9379 and −0.9639 for the single-line data, and −0.9446 and −0.9795 for the planar data. Meanwhile, a positive correlation is observed between K and z_0, with coefficients of 0.8998 and 0.8931, respectively.

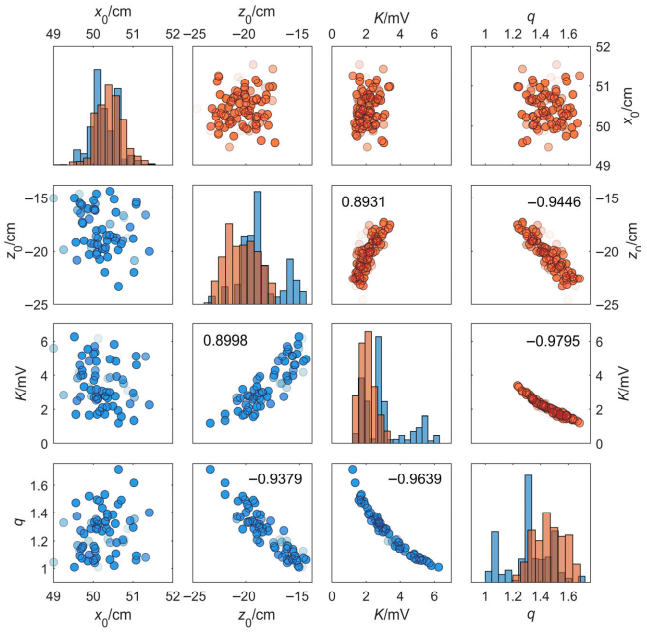


Figure 10. MCMC solutions from laboratory SP data. The on-diagonal plots represent the posterior probability distribution of model parameters, and the off-diagonal scatterplots represent the pairwise correlations in the MCMC sampling (blue for single-line data and orange for planar data).

5. Conclusions

This study employed an adaptive MCMC algorithm within the Bayesian framework to evaluate the performance of planar SP data, in comparison with single-line data, in reconstructing model parameters and reducing associated uncertainties. The analysis was conducted using two synthetic cases and a raw SP dataset obtained from a redox monitoring experiment on a spherical iron–copper model. The stochastic inversion results provided information on the sensitivity of the distribution and polarization intensity of subsurface targets. Numerical outcomes show that the parameter x_0 can be reliably estimated, with relative deviations from the true values remaining below 3%. In contrast, the accuracy in estimating parameter K is much lower than other parameters, and is associated with a larger uncertainty, as reflected by an average relative length of the 95% credible interval exceeding 70%. Comparisons across datasets with different volumes indicate that the use of planar data reduces the uncertainty of estimated parameters by 40%~50%, while the relative difference of the parameters decreases by 70%~75%. Note that the quantitative conclusions drawn here are specific to the models and datasets employed in this work. In addition, extending the analytical solution to 3D space and adapting it to other non-vertically polarized models currently presents challenges in mathematical derivation.

Author Contributions: Conceptualization, L.Z. and J.X.; methodology, J.X.; software, L.Z. and J.X.; validation, L.Z., S.F. and J.X.; formal analysis, L.Z. and S.F.; investigation, L.Z. and S.F.; resources, J.X.; data curation, L.Z. and J.X.; writing—original draft preparation, L.Z., S.F. and J.X.; writing—review and editing, L.Z., S.F., S.X., D.H., H.L., Y.S. and J.X.; visualization, L.Z., S.F. and J.X.; supervision, J.X.; project administration, J.X.; funding acquisition, L.Z. and S.F. All authors have read and agreed to the published version of the manuscript.

Funding: This research was funded by Hezhou University Doctoral Scientific Research Initiation Grant (grant number 2025BSQD06) and 2024 Guangxi Housing and Urban-Rural Construction Science and Technology Plan Project (Scientific Research and Development Category, No. 32).

Data Availability Statement: The data presented in this study are available on request from the corresponding authors. The data are not publicly available due to the centrality of the dataset to our ongoing research and its current active analysis. It will be shared after the main findings are published to protect research integrity and priority.

Conflicts of Interest: The authors declare no conflicts of interest.

References

1. Toro, N.; Robles, P.; Jeldres, R.I. Seabed mineral resources, an alternative for the future of renewable energy: A critical review. *Ore Geol. Rev.* **2020**, *126*, 103699. [CrossRef]
2. Vysetti, B. Deep-sea mineral deposits as a future source of critical metals, and environmental issues—A brief review. *Miner. Miner. Mater.* **2023**, *2*, 5. [CrossRef]
3. Miller, K.A.; Thompson, K.F.; Johnston, P.; Santillo, D. An overview of seabed mining including the current state of development, environmental impacts, and knowledge gaps. *Front. Mar. Sci.* **2018**, *4*, 418. [CrossRef]
4. Ma, W.; Zhang, K.; Du, Y.; Liu, X.; Shen, Y. Status of sustainability development of deep-sea mining activities. *J. Mar. Sci. Eng.* **2022**, *10*, 1508. [CrossRef]
5. Yao, W.; Tian, C.; Teng, Y.; Diao, F.; Du, X.; Gu, P.; Zhou, W. Development of deep-sea mining and its environmental impacts: A review. *Front. Mar. Sci.* **2025**, *12*, 1598584. [CrossRef]
6. Wu, C.; Zou, C.; Peng, C.; Liu, Y.; Wu, T.; Zhou, J.; Tao, C. Numerical simulation study on the relationships between mineralized structures and induced polarization properties of seafloor polymetallic sulfide rocks. *Minerals* **2022**, *12*, 1172. [CrossRef]
7. Yang, Y.; Zhang, G.; Yao, C.; Deng, Z.; Ren, Z.; Li, C. Application of induced polarization method in mineral resource exploration. *Sustainability* **2023**, *15*, 3840. [CrossRef]
8. Ishizu, K.; Goto, T.; Ohta, Y.; Kasaya, T.; Iwamoto, H.; Vachiratienchai, C.; Siripunvaraporn, W.; Tsuji, T.; Kumagai, H.; Koike, K. Internal structure of a seafloor massive sulfide deposit by electrical resistivity tomography, Okinawa Trough. *Geophys. Res. Lett.* **2019**, *46*, 11025–11034. [CrossRef]

9. Kasaya, T.; Iwamoto, H.; Kawada, Y.; Hyakudome, T. Marine DC resistivity and self-potential survey in the hydrothermal deposit areas using multiple AUVs and ASV. *Terr. Atmos. Ocean. Sci.* **2020**, *31*, 579–588. [CrossRef]
10. Gehrmann, R.A.S.; North, L.J.; Graber, S.; Szitkar, F.; Petersen, S.; Minshull, T.A.; Murton, B.J. Marine mineral exploration with controlled source electromagnetics at the TAG hydrothermal field, 26°N mid-Atlantic ridge. *Geophys. Res. Lett.* **2019**, *46*, 5808–5816. [CrossRef]
11. Ishizu, K.; Kasaya, T.; Goto, T.-N.; Koike, K.; Siripunvaraporn, W.; Iwamoto, H.; Kawada, Y.; Ishibashi, J.-I. A marine controlled-source electromagnetic application using towed and seafloor-based receivers capable of mapping seafloor and embedded massive sulfides. *Geophysics* **2024**, *89*, 1MJ-V305. [CrossRef]
12. Zhang, B.; Qu, K.; Yin, C.; Wang, Y.; Liu, Y.; Ren, X.; Su, Y. Review of 3D electromagnetic modeling and inversion for mineral exploration. *Geophysics* **2025**, *90*, E87–E99. [CrossRef]
13. Araya, A.; Kanazawa, T.; Shinohara, M.; Yamada, T.; Fujimoto, H.; Iizasa, K.; Ishihara, T. Gravity gradiometer implemented in AUV for detection of seafloor massive sulfides. In Proceedings of the 2012 Oceans, Hampton Roads, VA, USA, 14–19 October 2012.
14. Honsho, C.; Yamazaki, T.; Ura, T.; Okino, K.; Morozumi, H.; Ueda, S. Magnetic anomalies associated with abundant production of pyrrhotite in a sulfide deposit in the Okinawa Trough, Japan. *Geochem. Geophys. Geosyst.* **2016**, *17*, 4413–4424. [CrossRef]
15. Kawada, Y.; Kasaya, T. Marine self-potential survey for exploring seafloor hydrothermal ore deposits. *Sci. Rep.* **2017**, *7*, 13552. [CrossRef] [PubMed]
16. Zhu, Z.; Tao, C.; Shen, J.; Revil, A.; Deng, X.; Liao, S.; Zhou, J.; Wang, W.; Nie, Z.; Yu, J. Self-potential tomography of a deep-sea polymetallic sulfide deposit on southwest Indian ridge. *J. Geophys. Res. Solid Earth* **2020**, *125*, e2020JB019738. [CrossRef]
17. Su, Z.; Tao, C.; Zhu, Z.; Revil, A.; Shen, J.; Nie, Z.; Li, Q.; Deng, X.; Zhou, J.; Liu, L. Joint interpretation of marine self-potential and transient electromagnetic survey for seafloor massive sulfide (SMS) deposits: Application at TAG hydrothermal mound, Mid-Atlantic Ridge. *J. Geophys. Res. Solid Earth* **2022**, *127*, e2022JB024496. [CrossRef]
18. Xie, J.; Cui, Y.; Liu, J.; Guo, Y.; Zhang, L.; Luo, Y.; Zhang, P. A review on theory, modeling, inversion, and application of self-potential in marine mineral exploration. *Trans. Nonferrous Met. Soc. China* **2023**, *33*, 1214–1232. [CrossRef]
19. Biswas, A. A review on modeling, inversion and interpretation of self-potential in mineral exploration and tracing paleo-shear zones. *Ore Geol. Rev.* **2017**, *91*, 21–56. [CrossRef]
20. Mehanee, S.A. Simultaneous joint inversion of gravity and self-potential data measured along profile: Theory, numerical examples, and a case study from mineral exploration with cross validation from electromagnetic data. *IEEE Trans. Geosci. Remote. Sens.* **2022**, *60*, 4701620. [CrossRef]
21. Mehanee, S.A. An efficient regularized inversion approach for self-potential data interpretation of ore exploration using a mix of logarithmic and non-logarithmic model parameters. *Ore Geol. Rev.* **2014**, *57*, 87–115. [CrossRef]
22. Biswas, A.; Sharma, S.P. Interpretation of self-potential anomaly over idealized body and analysis of ambiguity using very fast simulated annealing global optimization. *Near Surf. Geophys.* **2015**, *13*, 179–195. [CrossRef]
23. Fedi, M.; Abbas, M.A. A fast interpretation of self-potential data using the depth from extreme points method. *Geophysics* **2013**, *78*, E107–E116. [CrossRef]
24. Kawada, Y.; Kasaya, T. Self-potential mapping using an autonomous underwater vehicle for the Sunrise deposit, Izu-Ogasawara arc, southern Japan. *Earth, Planets Space* **2018**, *70*, 142. [CrossRef]
25. Constable, S.; Kowalczyk, P.; Bloomer, S. Measuring marine self-potential using an autonomous underwater vehicle. *Geophys. J. Int.* **2018**, *215*, 49–60. [CrossRef]
26. Zhu, Z.; Shen, J.; Tao, C.; Deng, X.; Wu, T.; Nie, Z.; Wang, W.; Su, Z. Autonomous-underwater-vehicle-based marine multi-component self-potential method: Observation scheme and navigational correction. *Geosci. Instrum. Methods Data Syst.* **2021**, *10*, 35–43. [CrossRef]
27. Su, Z.; Tao, C.; Shen, J.; Revil, A.; Zhu, Z.; Deng, X.; Nie, Z.; Li, Q.; Liu, L.; Wu, T.; et al. 3D self-potential tomography of seafloor massive sulfide deposits using an autonomous underwater vehicle. *Geophysics* **2022**, *87*, B255–B267. [CrossRef]
28. Ahmed, A.S.; Jardani, A.; Revil, A.; Dupont, J. SP2DINV: A 2D forward and inverse code for streaming potential problems. *Comput. Geosci.* **2013**, *59*, 9–16. [CrossRef]
29. Mendonça, C.A. Forward and inverse self-potential modeling in mineral exploration. *Geophysics* **2008**, *73*, F33–F43. [CrossRef]
30. Sheffer, M.R.; Oldenburg, D.W. Three-dimensional forward modelling of streaming potential. *Geophys. J. Int.* **2007**, *169*, 839–848. [CrossRef]
31. Elhussein, M. A novel approach to self-potential data interpretation in support of mineral resource development. *Nat. Resour. Res.* **2021**, *30*, 97–127. [CrossRef]
32. Rao, K.; Jain, S.; Biswas, A. Global optimization for delineation of self-potential anomaly of a 2D inclined plate. *Nat. Resour. Res.* **2021**, *30*, 175–189. [CrossRef]
33. Abdelazeem, M.; Gobashy, M.; Khalil, M.H.; Abdrabou, M. A complete model parameter optimization from self-potential data using Whale algorithm. *J. Appl. Geophys.* **2019**, *170*, 103825. [CrossRef]

34. Xie, J.; Cui, Y.; Niu, Q. Coupled inversion of hydraulic and self-potential data from transient outflow experiments to estimate soil petrophysical properties. *Vadose Zone J.* **2021**, *20*, e20157. [CrossRef]
35. Younes, A.; Zaouali, J.; Lehmann, F.; Fahs, M. Sensitivity and identifiability of hydraulic and geophysical parameters from streaming potential signals in unsaturated porous media. *Hydrol. Earth Syst. Sci.* **2018**, *22*, 3561–3574. [CrossRef]
36. Vrugt, J.A.; Gupta, H.V.; Bouten, W.; Sorooshian, S. A shuffled complex evolution Metropolis algorithm for optimization and uncertainty assessment of hydrologic model parameters. *Water Resour. Res.* **2003**, *39*, 1201. [CrossRef]
37. Haario, H.; Saksman, E.; Tamminen, J. An adaptive Metropolis algorithm. *Bernoulli* **2001**, *7*, 223–242. [CrossRef]
38. Revil, A.; Su, Z.; Zhu, Z.; Maineult, A. Self-Potential as a tool to monitor redox reactions at an ore body: A sandbox experiment. *Minerals* **2023**, *13*, 716. [CrossRef]
39. Xie, J.; Cui, Y.; Guo, R.; Chen, H.; Guo, Y.; Liu, J. A deep learning algorithm for locating contaminant plumes from self-potential: A laboratory perspective. *IEEE Trans. Geosci. Remote. Sens.* **2025**, *63*, 5902913. [CrossRef]
40. Ahmad, Z. *Principles of Corrosion Engineering and Corrosion Control*; Elsevier: Amsterdam, The Netherlands, 2006; pp. 352–381.

Disclaimer/Publisher's Note: The statements, opinions and data contained in all publications are solely those of the individual author(s) and contributor(s) and not of MDPI and/or the editor(s). MDPI and/or the editor(s) disclaim responsibility for any injury to people or property resulting from any ideas, methods, instructions or products referred to in the content.